

Investigation of intermittent motion mechanisms in large landslides based on in-situ monitoring and microtremor survey[☆]

Yang Jian ^{a,b}, Zhang Huiqi ^a, Jian Wenbin ^{a,b}, Lin Lipeng ^a, Luis F. Robledo ^c, Wang Hao ^{a,b}, Dou Hongqiang ^{a,b}

^a Department of Geotechnical and Geological Engineering, Fuzhou University, Fuzhou, 350108, China

^b Engineering Research Center of Geological Engineering, Fuzhou University, Fuzhou, 350108, China

^c Universidad Andres Bello, Santiago, 7500971, Chile

ARTICLE INFO

Keywords:

Intermittent motion
Microtremor survey
In-situ monitoring
Internal structures
Preferential flow pathways

ABSTRACT

The Yaoshan landslide, situated in the hilly and mountainous terrain of southeastern China, exhibits typical episodic sliding behavior driven by a complex subsurface hydrogeological system. This study integrates long-term in-situ monitoring data with microtremor survey techniques to investigate the internal mechanisms underlying its intermittent movement. A two-dimensional apparent S-wave velocity (V_x) structure was constructed for the key sliding area, revealing both lateral and vertical discontinuities associated with lithological boundaries and potential slip surfaces. By correlating low-velocity anomalies with borehole lithology and observed deep-seated deformation features, the depth and geometry of the principal slip surface were identified. Several geophysical cross-sections revealed bowl-shaped depressions within the landslide mass, where interconnected low-velocity zones likely function as preferential hydrological pathways. Monitoring data indicate that these depressions are prone to rapid pore water pressure buildup during intense rainfall, which can trigger reactivation of sliding. Field surveys further verified the hydraulic connectivity between low-velocity zones and surface gullies, suggesting strong coupling between surface runoff and internal groundwater flow. The perennial flow in gullies, combined with long-term seepage through colluvial deposits, may accelerate internal erosion within the slip zone. These findings offer new insights into the hydro-mechanical coupling mechanisms of landslides and provide a scientific foundation for risk assessment and the design of mitigation measures in geologically similar settings.

1. Introduction

Landslides are a common natural disaster worldwide that severely impact the environment and human activities. In the southeastern hilly regions of China, typhoons and heavy rainfall trigger numerous landslides annually, leading to significant casualties and economic losses (Zhuang et al., 2023, 2022). Comprehensive field investigations are critical for mitigating and reducing landslide risks. The geological structure of the landslide body and the characteristics of subsurface hydrodynamics are the major factors influencing the evolution of landslides (Huang and Li, 2011; Luo et al., 2019; Osawa et al., 2023; Zhang et al., 2023). Although traditional direct field techniques, such as geological surveys, yield direct information on soil properties and landslide activity, they have limitations such as their invasive nature, high cost, and limited spatial representativeness (Pazzi et al., 2019; Hasan et al., 2023).

In intermittent landslides with complex geological structures and variable hydrological characteristics (Lacroix et al., 2020; Krzeminska et al., 2013), preferential hydrological pathways and internal erosion phenomena may develop within the slope body (Skempton and Hutchinson, 1969; Handwerger et al., 2013; Nappo et al., 2019; Carey et al., 2019). This can lead to significant errors when relying on the use of limited boreholes for surveys (Luo et al., 2019). Such methods can only provide geotechnical layer information at discrete locations (e.g., borehole logs), and the positioning of these layers generally depends on engineering judgment between the existing discrete test sites. As a result, a major limitation of the current landslide investigation methods is the lack of information on the spatial variability of internal structural characteristics across the landslide area. This information is critical for an in-depth understanding of seepage paths and movement mechanisms of landslides, yet it has not been adequately addressed in the existing literature.

[☆] This document is the results of the research project funded by the National Natural Science Foundation of China (U2005205) (41861134011).

* Corresponding author.

E-mail address: jwb@fzu.edu.cn (Jian W.).

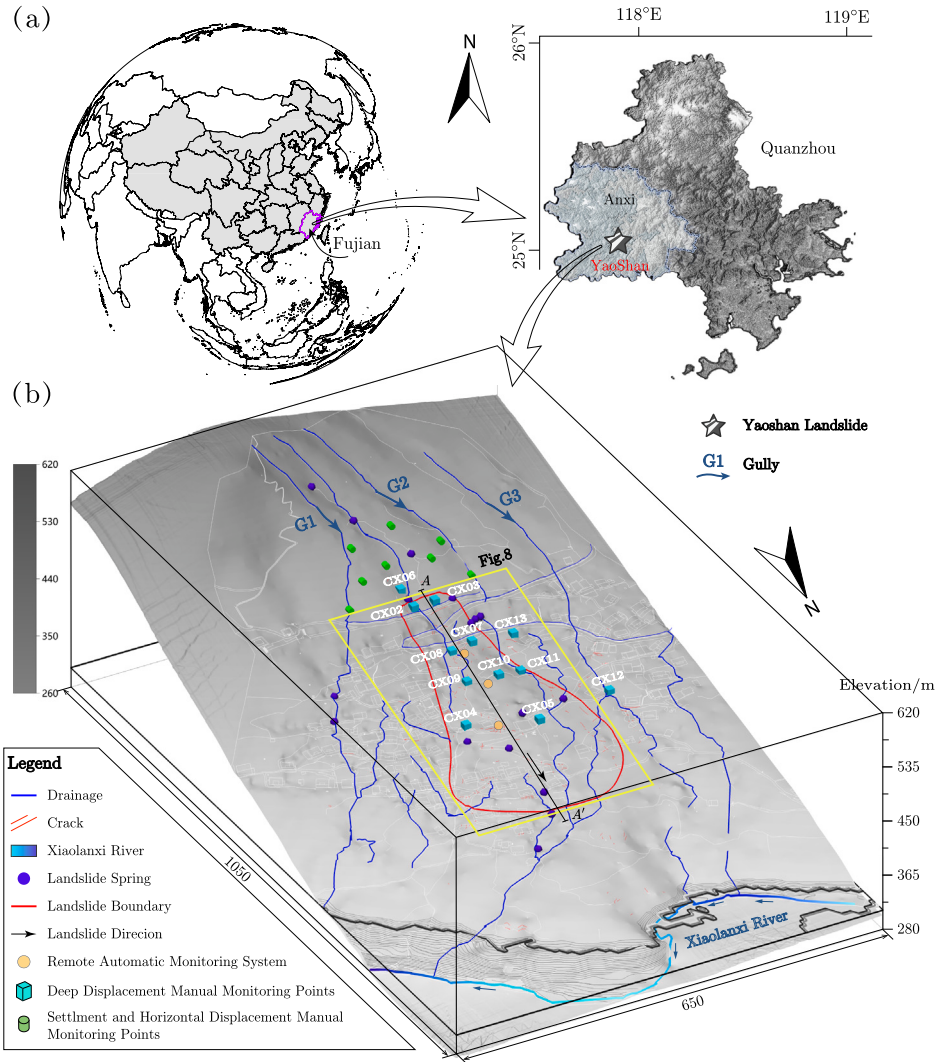


Fig. 1. (a) Specific location of the Yaoshan landslide. (b) Three-dimensional model of the Yaoshan landslide, indicating key survey information (landslide deformation boundary, gullies (G1–G3), roads, water systems, and buildings), monitoring point layout, and the area in Fig. 8 (marked by a yellow rectangle). (For interpretation of the references to color in this figure legend, the reader is referred to the web version of this article.)

To address this gap, geophysical methods capable of resolving spatially continuous subsurface features have gained prominence. Their non-invasive nature, relatively low cost, and high data coverage make them an effective complement to traditional investigations (Rahimi et al., 2018; Perrone et al., 2021; Pazzi et al., 2019; Calamita et al., 2023b). Among these, seismic techniques—particularly seismic refraction and multichannel analysis of surface waves (MASW)—have proven valuable in mapping near-surface stratigraphy and detecting hydrogeological boundaries through P- and S-wave velocity profiles (Dai et al., 2023; Kamiński et al., 2021; Lu et al., 2024; Roberts and Asten, 2005; Fabbrocino et al., 2015). Such contrasts are widely used to delineate landslide masses and identify saturated zones (Berti et al., 2019; Peng et al., 2017).

Recently, microtremor survey methods (MSM), based on ambient vibration analysis, have emerged as powerful tools for investigating near-surface structures without requiring controlled sources or ideal terrain (Ling, 1994; Okada, 2006; Xu et al., 2012). The technique is particularly useful in mountainous or vegetated regions where conventional seismic surveys are difficult to deploy. Its potential for detecting hidden internal layers and weak zones has been highlighted in several case studies (Li et al., 2024; Su et al., 2017).

This study presents a novel approach to characterizing the internal architecture and hydromechanical behavior of intermittent large-scale landslides, addressing key gaps in understanding the coupling between subsurface structures and preferential hydrological pathways. We systematically applied the MSM to the Yaoshan landslide in southeastern China, integrating high-resolution V_x imaging with detailed field investigations and long-term in-situ monitoring data. The results reveal critical subsurface structures, the spatial distribution of potential hydrological conduits, and the spatiotemporal dynamics of slope deformation. Our results demonstrate that MSM provides a non-invasive and efficient means of identifying internal heterogeneities and concealed hydrological pathways that govern landslide behavior. This approach improves understanding of landslide evolution and offers a practical framework for early warning, structural assessment, and hazard mitigation in complex geological settings.

2. Geography and geology

2.1. Geographical and geomorphological setting

The Yaoshan landslide is located in Anxi County, Fujian Province, China, approximately 8 km east of Xiping Town (Fig. 1a). It lies within

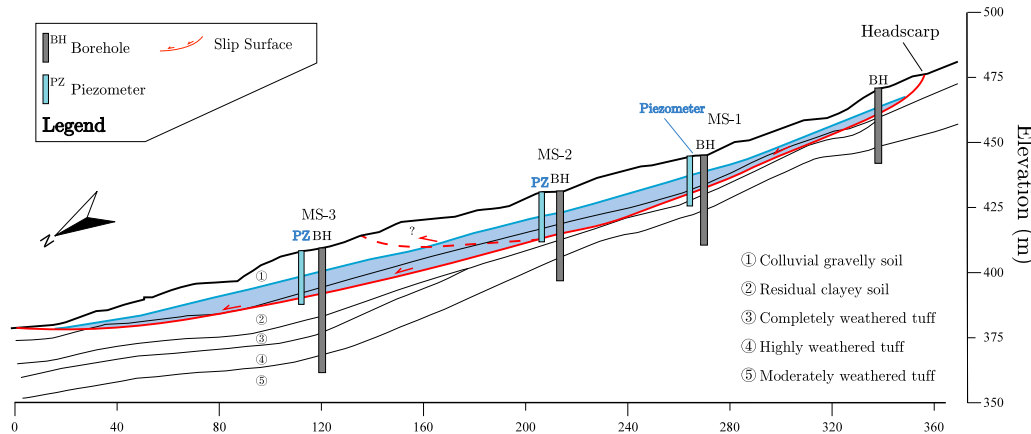


Fig. 2. Engineering geological profile along main sliding surface A – A' in Fig. 1b.

a tectonic erosion mid-to low-mountain terrain zone (Fig. 1b). The landslide body is situated on the lower slope section of a hillside, with pronounced topographic relief and elevation ranging from 350 to 472 m. The landslide exhibits a typical tongue-shaped morphology, with a combination of gentle and steep slope segments from the rear to the front edge. The main sliding direction is N10°E, and the overall slope angle ranges between 20° and 30°. Three major gullies (Fig. 1b, G1–G3) are developed within the landslide area, each with varying incision depths and widths. The eastern (G1) and western (G3) gullies are deeply incised, with widths of approximately 10 m and depths of around 5 m, while the central gully (G2) is comparatively shallow. All three gullies carry perennial water flow, with an estimated annual average discharge of 150–300 m³/d, serving as a significant source of subsurface water recharge within the landslide body and playing a crucial role in its hydrogeological evolution.

Since 2000, the area has shown clear signs of deformation and damage under repeated episodes of intense rainfall. The most severe manifestations occurred during Typhoon Meranti (Typhoon No. 14) and Typhoon Megi (Typhoon No. 17) in 2016. Surface deformation features included cracking and collapse of residential buildings, longitudinal fissures in roads, tilting of electrical infrastructure, and the development of bead-like subsidence pits and water springs. These phenomena pose significant threats to over 1100 residents, hundreds of homes, and critical infrastructure such as power lines, roads, and cultural heritage sites (including the birthplace of Tieguanyin tea), with an estimated potential economic loss exceeding 50 million RMB (Liu et al., 2021).

2.2. Geological and lithological characteristics

The landslide area exposes extensive Late Jurassic tuff and tuffaceous lava formations (J_3n^c). Approximately 800 m north of the site, a NE30° normal fault is developed, dipping southeastward at an angle of 60–70°, along which granite porphyry dikes have intruded the fractured zone. Core drilling reveals fault breccia cemented with fault gouge (Fig. 12c), with very low core recovery due to pervasive fracturing and groundwater leakage along the entire borehole.

The stratigraphic sequence in the landslide area, from top to bottom, consists of colluvial gravelly soil, residual clayey soil, completely weathered tuff, highly weathered tuff, and moderately weathered tuff (Fig. 2). The landslide movement is primarily controlled by the interface between the residual clayey soil and the weathered tuff. The residual clayey soil layer (2.0–12.0 m thick) is yellowish-brown, ranging from plastic to hard plastic in consistency, loosely structured, containing iron–manganese nodules, and characterized by low permeability and strength, making it a typical weak layer. Beneath it, the completely and highly weathered tuff (combined thickness up to 17.8 m) is highly fragmented and clay-rich, with low shear strength

and locally developed clay-rich shear zones, which are potential sliding surfaces. The moderately weathered tuffaceous lava, serving as the regional bedrock (J_3n^c), is hard, with few fractures and favorable mechanical properties.

Due to the loose structure of the overlying sliding mass, suspended structures exist within it, and a well-developed subsurface water seepage network is present. Consequently, the vertical evolution of seepage pathways within the landslide is critical for its stability assessment (Yang et al., 2024).

3. Data and methods

3.1. In-situ monitoring of landslide multi-physical fields

The relationship between the deformation and hydrological characteristics of the Yaoshan landslide was examined by regular manual monitoring of horizontal displacement, settlement, and deep displacement. The monitoring was conducted from March 15, 2018, to December 15, 2019, with a total of 23 deep soil lateral displacement monitoring sessions, 16 water level monitoring sessions, and 10 horizontal displacement and settlement monitoring sessions.

Eight points were established for both horizontal displacement and settlement monitoring. Cement nails were driven into fixed markers, with steel markers measuring $\Phi 14$ mm × 200 mm serving as observation points. Three stable and reliable monitoring base points (T1 to T3) were established outside the deformation zone. Moreover, 13 inclinometer and water level pipes were installed, with the lower parts perforated and wrapped in 60-mesh filters to ensure water permeability (Fig. 1b).

In August 2019, an automated multi-physical field monitoring system was set up to monitor landslides (Fig. 3). This system included rain gauges, pore water pressure sensors, array-type inclinometers, and water level meters, all installed at central positions on the main sliding surface (MS-1, MS-2) for real-time, long-term monitoring. Data from each sensor was recorded every hour and transmitted in real time to the monitoring system.

3.2. Microtremor survey methods

The MSM assumes that microseisms are stationary random processes in both space and time (Aki, 1957). The spatial autocorrelation (SPAC) method for MSM analysis derives the dispersion characteristics of Rayleigh waves from the vertical components of microseisms recorded by multiple seismometers deployed on-site. In MSM, the S-wave velocity structure of lithological layers and geological formations is inverted using SPAC (Aki, 1957; Okada, 2006; Xu et al., 2012). It is

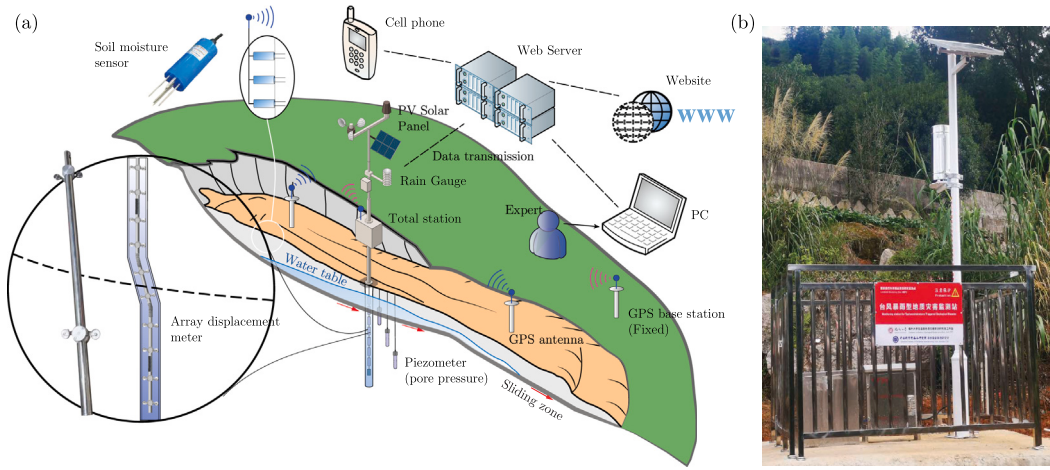


Fig. 3. (a) Remote automated monitoring system. (b) Photographs of on-site monitoring stations.

currently considered one of the most effective methods for determining shear wave velocities in sedimentary layers.

An important step in the microtremor array surveying method is how to extract surface wave dispersion curves from recorded data using the observation array. The SPAC method calculates the waveform correlation $r_{ox}(\omega, r, \theta)$ between the array center $O(0, 0)$ of the circular array and each receiver point $x(r, \theta)$ on the circumference with radius r using the complex coherence function (Fig. 4a).

$$r_{ox}(\omega, r, \theta) = \frac{R_e [S_{ox}(\omega, r, \theta)]}{\sqrt{S_o(\omega) S_x(\omega, r, \theta)}} \quad (1)$$

where $S_{ox}(\omega, r, \theta)$ denotes the cross-power spectrum between the array center point O and the point x on the circumference. R_e represents the real part of the complex function $S_{ox}(\omega, r, \theta)$. The parameter ω is the angular frequency, θ is the azimuthal angle, and r is the radius of the circular array. $S_o(\omega)$ and $S_x(\omega, r, \theta)$ are the power spectral densities of the microtremor data recorded at the array center point O and the peripheral point x , respectively.

By utilizing the property that the average value of the spatial autocorrelation coefficient equals the value of the Bessel function (Fig. 4b), the SAC coefficient can be obtained:

$$\rho(\omega, r) = \frac{1}{2\pi} \int_0^{2\pi} r_{ox}(\omega, r, \theta) d\theta = J_0(kr) \quad (2)$$

where $\rho(\omega, r)$ is the SAC coefficient, J_0 is the zero-order Bessel function of the first kind, $k = 2\pi\omega/c(\omega)$ is the wavenumber (frequency divided by phase velocity), and $c(\omega)$ is the Rayleigh wave phase velocity.

The Rayleigh wave phase velocity is obtained from the inverse function of the Bessel function (Fig. 4c):

$$c(\omega) = 2\pi\omega \frac{r}{J_0^{-1}[\rho(\omega, r)]} \quad (3)$$

where J_0^{-1} is the inverse of the J_0 function.

Practical results have shown that for geological anomalies such as low-velocity or high-velocity interlayers, V_x is more sensitive than V_r (Fig. 5). Therefore, V_x is more effective in revealing subtle variations in subsurface structures (such as shear zones within landslides, preferential hydrological conduits, etc.). In practical applications, the Rayleigh wave phase velocity dispersion curve ($V_r - \omega$) is converted into a depth-dependent apparent S-wave velocity distribution curve ($V_x - h$) using the following Eq. (4). Then, by performing lateral interpolation and smoothing of the $V_x - h$ curves from multiple measurement points, a 2D V_x profile can be obtained. The inversion error is generally controlled within 10% compared to borehole data.

$$V_{x,i} = \left(\frac{t_i \cdot v_{r,i}^4 - t_{i-1} \cdot v_{r,i-1}^4}{t_i - t_{i-1}} \right)^{1/4} \quad (4)$$

where V_r is the phase velocity of the Rayleigh wave, and t_i is the period of the Rayleigh wave. V_x differs from V_r and V_s , and is typically referred to as the apparent S-wave velocity.

The SPAC method involves arranging microtremor sensors in a circular observation array. Fig. 6a shows the observation system used for microtremor detection, featuring a set of IGU-BD3C-5 microseismic measuring instruments. The observation system employed a hexagonal array, with S1 as the central measurement point and the remaining six points (S2-S7) as station points. These six microtremor observation points were uniformly distributed along the circumference of a circle with a radius R . Typically, the detection depth of the SPAC method is 3 to 5 times the observation radius. Preliminary geological surveys and monitoring indicated the maximum thickness of the landslide to be approximately 17 m. Therefore, an array radius of 5 m was chosen to achieve the appropriate SPAC detection depth.

The observation system employed seven microtremor sensors to capture digital signals simultaneously, synchronized by GPS clocks embedded in the data acquisition units. The data was independently collected at each observation point, with GPS automatically ensuring synchronization and time correction, ensuring a 2-h observation at each point. Based on the required detection depth and terrain variations, a series of measurement points were established (Xu et al., 2012, 2017), resulting in the development of a two-dimensional subsurface phase velocity structure model through continuous measurements. The SPAC method analyzed data from microtremor sensors 2–7 to determine the average phase velocity around instrument 1. The MSM chain array, as shown in Fig. 6b, c, allows for the concurrent measurement of average phase velocity beneath instruments 1, 3, 9, and 12. In the second round of measurements, instruments 5, 6, and 7 were placed at the positions of instruments 8, 9, and 10, respectively, while the other instruments remained in their original locations. This process ultimately yielded a continuous phase velocity-depth profile.

4. Results

4.1. Landslide deformation characteristics and mechanisms

The large landslide deformation area in Yaoshan Village exhibits a ‘tongue-shaped’ morphology. The landslide is approximately 400 m in length and 250 m in width, with the sliding zone depth ranging from 10–17 m (Fig. 8c). The area spans approximately 64,000 m², with a volume of about 650,000 m³. Based on field investigations and long-term deformation monitoring, the development characteristics of the large landslide in Yaoshan Village were evaluated, and the landslide was divided into three zones (Fig. 8a): the traction zone (Zone I), the main sliding zone (Zone II), and the toe zone (Zone III).

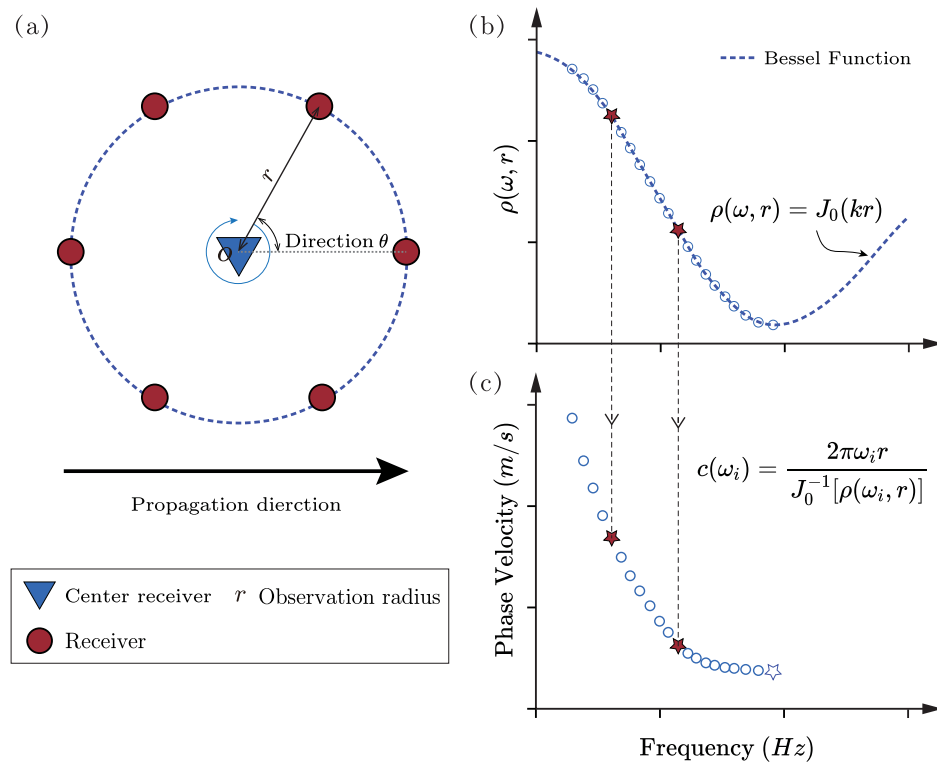


Fig. 4. Steps for obtaining dispersion curves using spatial autocorrelation (SAC) method: (a) Calculate the correlation between the central point and the peripheral points through a circular array. (b) Obtain the SAC coefficient using the Bessel function. (c) Retrieve the phase velocity using the inverse function of the Bessel function.

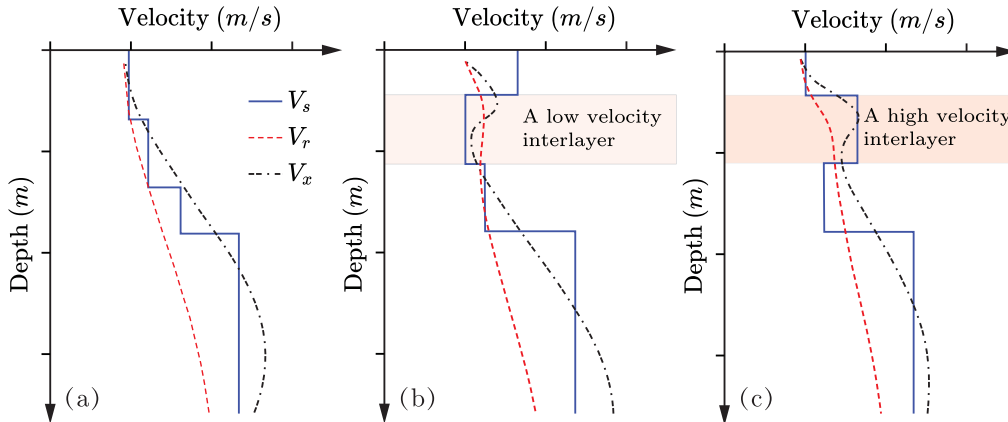


Fig. 5. Comparison of V_s , V_r , and V_x across different geological models (modified from Ling (1994)). (a) Under conditions of increasing velocity. (b) Within low-velocity interlayers (e.g., internal shear zones of the landslide, preferential hydrological conduits, karst cavities). (c) Within high-velocity interlayers (isolated boulders).

4.1.1. Deep deformation characteristics

Between May and June 2019, Anxi County in Quanzhou City experienced prolonged heavy rainfall, with cumulative rainfall reaching 251.8 mm in May and 323.4 mm in June (Fig. 7b), resulting in enhanced deformation of the Yaoshan landslide. To assess this deformation, monitoring data from 12 inclinometer boreholes were collected on three key dates in 2019: May 9, May 28, and June 28. Kriging interpolation was used to visualize the overall three-dimensional deformation of the landslide, and the temporal and spatial dynamics of the landslide deformation were further analyzed together with rainfall data. The displacement of the landslide was represented by a color gradient that ranged from blue (small displacement) to red (large displacement).

Fig. 7a shows the dynamic changes in the landslide area over different periods. With time, the cumulative deep displacement in the landslide area steadily increases, with the most significant displacement increment of 57.95 mm observed between May 28 and June 28. This is

a period when the cumulative rainfall reached 323.4 mm. This pattern reveals a strong correlation between landslide deformation and rainfall, with deep displacement exhibiting a pronounced exponential increase with increasing cumulative rainfall. Moreover, the main sliding area (Zone II) exhibits the most significant response to rainfall compared to other deformation zones (Fig. 7d, red curve), highlighting the dynamic influence of rainfall on the deformation across different sections of the landslide. Continuous monitoring of these critical deformation zones is essential for better understanding landslide mechanisms and enhanced risk assessment.

Fig. 7c shows the cumulative displacement over time at different monitoring points across various regions of the landslide. Displacement increases gradually at all monitoring points, indicating distinct zonal characteristics, though the degree of deformation varies. The main sliding area (Zone II) experiences the most significant soil displacement, while the traction deformation zone (Zone I) shows the least. This

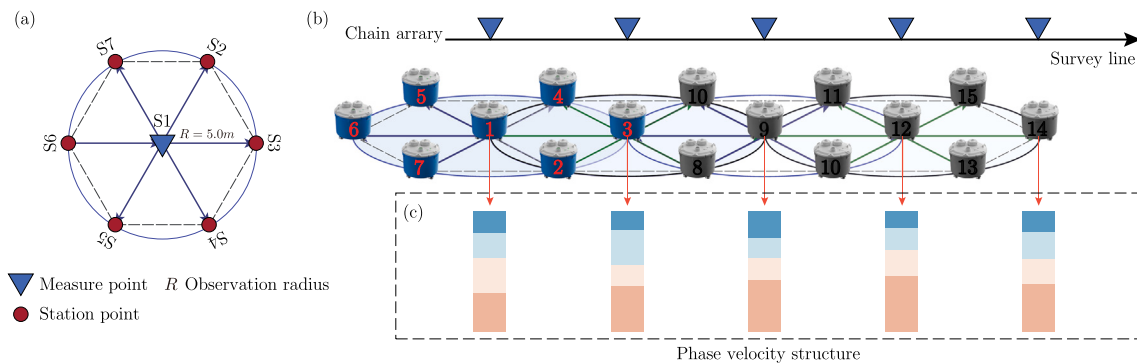


Fig. 6. Layout of the microtremor observation array. (a) Single-point array survey system. (b) Layout of the microtremor profile observation. (c) Determination of phase velocity-depth profile using microtremor chain array. Red solid circles indicate station points, and blue solid inverted triangles represent the locations of observation points. (For interpretation of the references to color in this figure legend, the reader is referred to the web version of this article.)

highlights the spatial variability in landslide movement and helps identify critical deformation zones. The box plot in Fig. 7e compares displacement changes across different landslide regions between May and June, revealing that displacement in June is significantly higher than that in May. This difference is primarily attributed to the longer duration and higher rainfall intensity in June and the continuous rainfall in May, which maintains high groundwater levels in the landslide area and delays the dissipation of pore water pressure within the slope. Additionally, the rear edge of the traction zone demonstrates notable subsidence, with some settlement exceeding horizontal displacement (Fig. 7f).

4.1.2. Crack development characteristics

The rear boundary of the traction zone (Zone I) in the slope deformation area is located at the beginning of the gentle slope terrace at an elevation of 472 m (Fig. 1a). This area features numerous cracks, primarily resulting from tensile and shear failure. Most of these cracks are oriented almost perpendicular to the road, with some intersecting to form jagged patterns. These subsidence-type tensile cracks measure 5 to 15 m in length, with openings of 5 to 15 cm and visible depths of 10 to 20 cm. Moreover, close to the cracks, especially on the side facing the free face, the rock and soil mass experiences downward displacement, with offsets of about 10 to 20 cm (Fig. 8b).

In the main sliding zone (Zone II), a majority of the cracks are aligned with the direction of landslide movement. Due to the slow movement of the landslide, these cracks are generally narrow and shallow, with the most visible cracks found along roads and ditches. Longer cracks are mainly distributed along the perimeter of the deformation zone. The front toe zone (Zone III) is predominantly affected by compressive and thrust deformation, characterized by numerous longitudinal radiating cracks aligned with the sliding direction (Fig. 8a) and expansion cracks perpendicular to the sliding direction. Visible signs of this deformation include bulging floors within buildings (Fig. 8d) and the appearance of feather-like and shear cracks in the shear zones along both sides.

4.1.3. Geometry of the landslide surface

The slip surface is the plane along which the soil or rock masses move during a landslide. Its direction, depth, and shape define the geometric characteristics of a landslide, providing insights into its potential movement patterns and associated hazards. Deep displacement data from 15 inclinometer boreholes over different periods revealed three slip surfaces (Fig. 9): the A-A' profile along the main sliding direction and the B-B' and C-C' profiles perpendicular to it. The main slip surface of the Yaoshan landslide (A-A' profile) exhibits a gentle slope of 22° to 25°, with an increase followed by a decrease in the landslide thickness along the sliding direction, and burial depths ranging from 12 to

17 m. This surface mainly occurs at the contact between sandy residual clay and completely weathered tuff, with a thickness of about 0.5 to 1.0 m. A distinct slip surface is observed in the main sliding zone (Zone II), with the C-C' profile reaching depths of 15 to 17 m (Fig. 8c CX8-9), indicating the distribution of deformation within a narrow shear zone. On the contrary, the traction zone (Zone I) lacks a fixed slip surface, with displacements at various depths typically inclining toward the landslide direction (Fig. 8c CX2), primarily influenced by the movement of the main sliding zone.

4.1.4. Landslide deformation mechanism

The intermittent movement of the Yaoshan landslide is impacted by the morphology of the slip surface, high pore pressure, and the reduction in effective stress along the slip surface (Fig. 10). The pore pressure on the slip surface fluctuates periodically as a result of seasonal variations in groundwater recharge (Fig. 10a), leading to intermittent movement marked by phases of acceleration and deceleration (Fig. 10b). The hydraulic head in the boreholes monitored in this study typically reaches its lowest level in winter, slightly increases in spring, and significantly increases again in summer due to frequent typhoon-induced rainfall in the hilly regions of southeastern China. This phenomenon is especially intense during this time of the year, leading to annual pore pressure fluctuations of up to 35 kPa. Notably, the pore water pressure in the sliding zone of the landslide responds rapidly to rainfall, resulting in rapid activation during rain and ceasing movement with the dissipation of pressure.

The probable reasons for this are (1) steep topography of the slope at the top and gentle at the bottom, with a catchment area of up to 800,000 m² in the rear mountain. This facilitates the recharge of surface and groundwater into the landslide deformation zone; (2) The loose structure of the surficial colluvial gravel layer, with several preferential pathways, facilitates rapid infiltration of surface water and migration of groundwater (Yang et al., 2024). The direct evidence for the existence of potential preferential hydrological pathways within the landslide is demonstrated later in the text through the interpretation of the landslide's internal structure using MSM.

4.2. Two-dimensional apparent S-wave velocity profile

To identify the subsurface structural characteristics along the key sections of the landslide, three MSM detection lines (D1-D3) were established in the main sliding zone (Zone II). This was based on the analysis of existing engineering geological data and a thorough evaluation of the Yaoshan landslide's deformation features. Each detection line was equipped with 23 and 19 microtremor detection points. The longest MSM profile, D1, is aligned with the main sliding direction of the landslide and measures 165 m, while D2 and D3 are perpendicular to the main sliding direction, with each measuring 135 m (Fig. 11a).

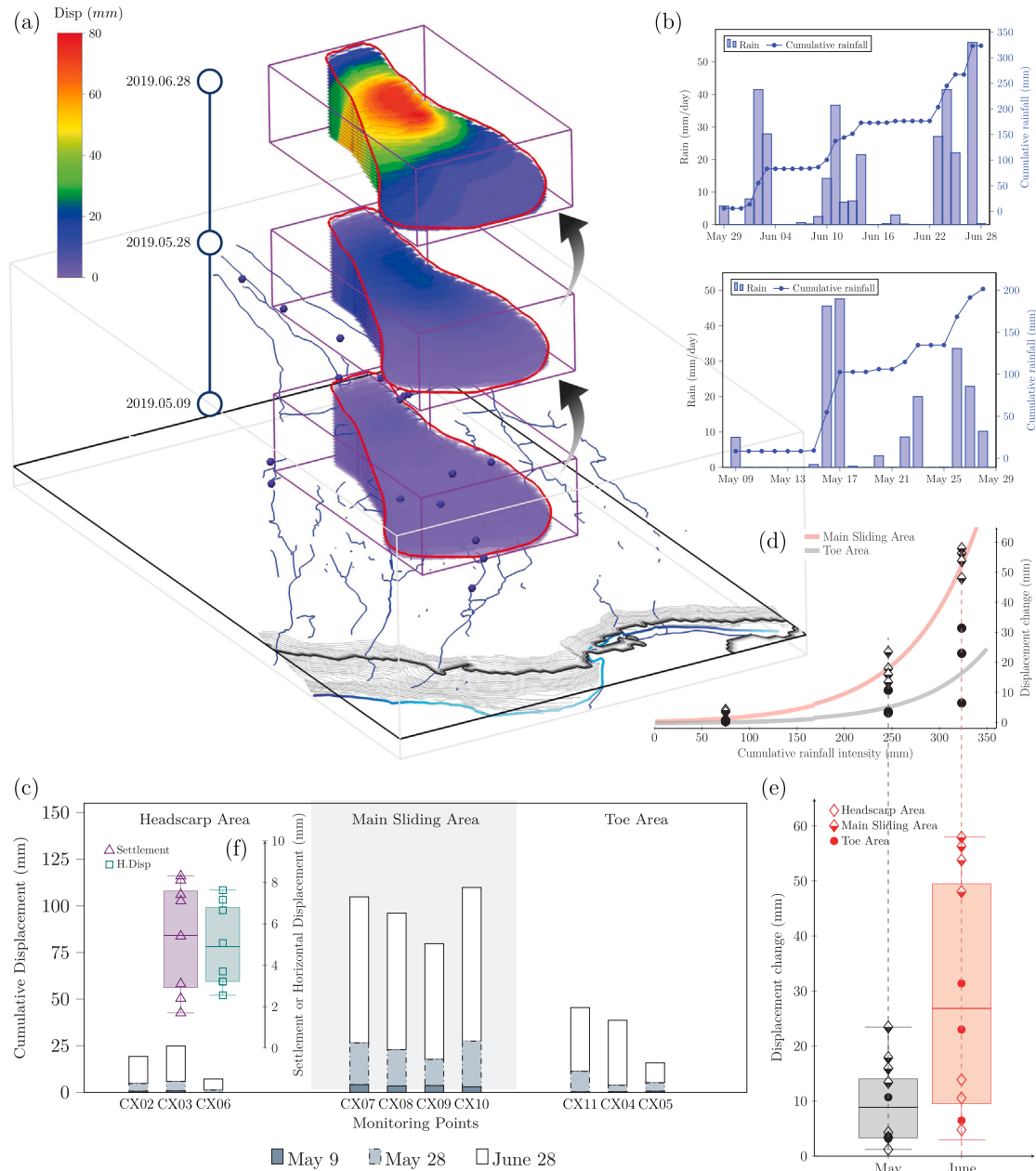


Fig. 7. Spatiotemporal distribution characteristics of overall deformation of the Yaoshan landslide during three different periods from May 9 to June 28, 2019. (a) Cumulative deep displacement at different periods. (b) Daily rainfall and cumulative rainfall for May and June. (c) Distribution patterns of cumulative deep displacement in different areas of the landslide. (d) Relationship between deep displacement changes and cumulative rainfall at each stage. (e) Distribution patterns of variations in deep displacement in different areas of the landslide during May and June. (f) Characteristics of settlement and horizontal displacement at the rear edge of the traction zone of the landslide. (For interpretation of the references to color in this figure legend, the reader is referred to the web version of this article.)

The interpretation of the 2D V_x profiles (Fig. 11b) was conducted based on the principle of progressing from the known to the unknown, using a combination of geological and geophysical information for comprehensive analysis. The first step involved superimposing collected borehole logs onto their corresponding positions on the profile for identification of lithological layers and their depths. Based on this method, the V_x range for each lithological layer was determined and used for tracking and interpreting these layers in the 2D microtremor profiles. Subsequently, a detailed analysis of the profile characteristics was conducted, considering factors such as velocity anomalies, background values, gradient changes, and morphology. This approach enabled the qualitative and quantitative interpretation of velocity anomalies (indicating lithological heterogeneity) and the delineation of lithological layers (interfaces) in the V_x profiles.

4.2.1. Lithological layer delineation

Based on the interpretation principles described above, the upper and lower boundaries of each lithological unit were delineated by correlating borehole-calibrated depths with profile features (Fig. 12). The geological structure of the landslide, from the surface to a depth of 25 m, can be sequentially divided into the colluvial gravelly soil layer, residual clayey soil layer, completely weathered tuff layer, and highly to moderately weathered tuff layer. Rock fragments 1–5 m in diameter were encountered in most boreholes, with several boulders observed at the slope surface and in excavated sections. These conditions result in marked heterogeneity from the surface colluvium down to the completely weathered tuff. The measured V_x profiles exhibit the following features:

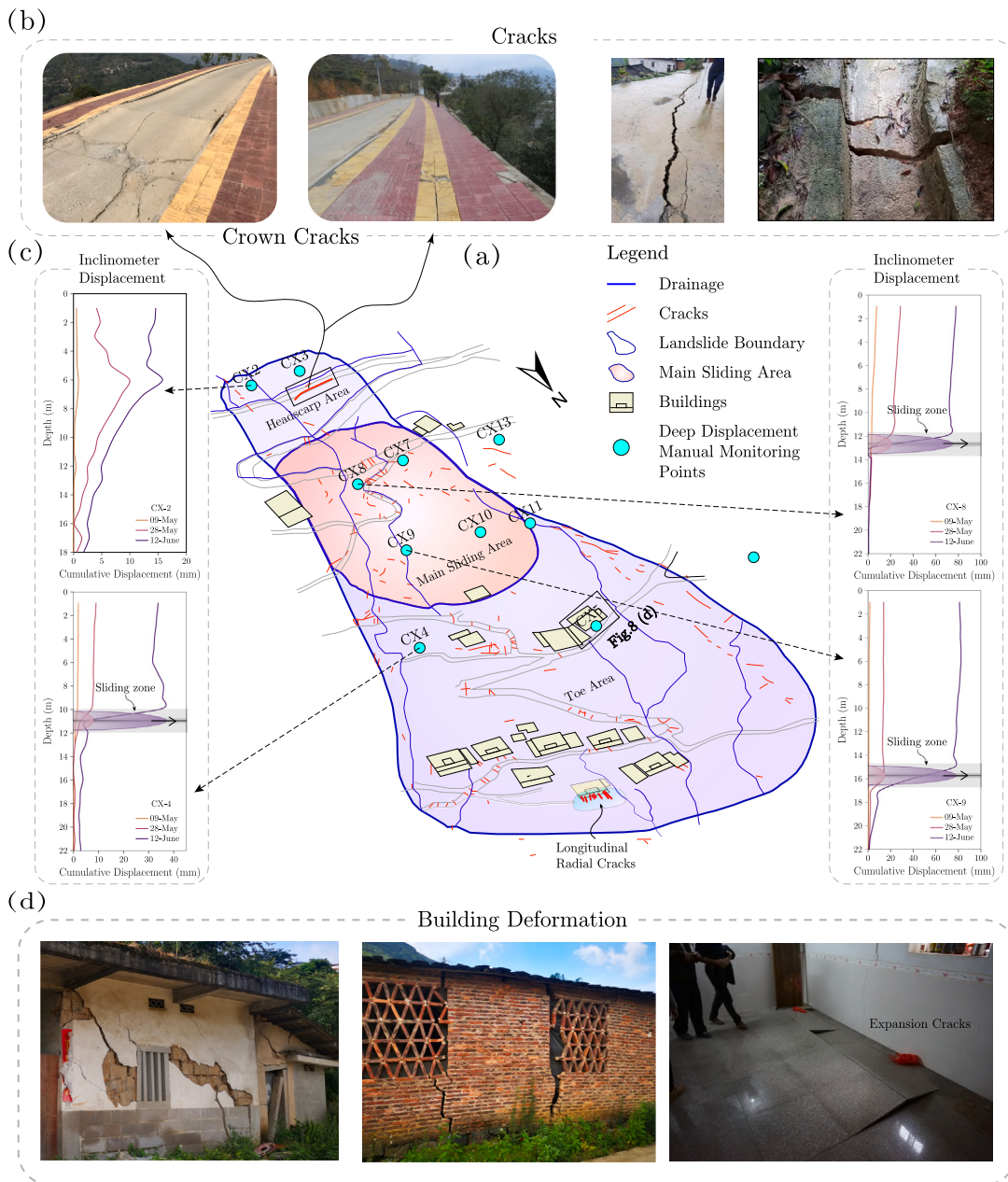


Fig. 8. (a) Deformation zones and crack characteristics of the Yaoshan landslide. (b) On-site photograph of tensile cracks on the road at the rear edge of the traction deformation zone (Zone I). (c) Cumulative deep inclinometer displacements in different landslide deformation zones. (d) Deformation characteristics of buildings in the toe zone (Zone III) of the landslide.

(1) Colluvial gravelly soil layer ($V_x < 270 \text{ m/s}$): The surface soil exhibits low V_x due to its composition—primarily colluvial clayey soil interspersed with boulders. Gravels (5–8 cm in diameter) account for approximately 50%–60% of the matrix and are loosely packed. Given the MSM system's limited resolution in the shallow subsurface (<10 m) due to its operational frequency range (0–10 Hz) (Xu et al., 2012, 2017), isolated boulders may not be reliably detected. The progressive increase in V_x with depth reflects the transition from unconsolidated surficial deposits to denser, less porous materials.

(2) Residual clayey soil layer ($270 \text{ m/s} < V_x < 350 \text{ m/s}$): The D3 profile revealed significant heterogeneity in the V_x distribution in the residual clayey soil layer. The bottom boundary of this layer gradually deepens toward the right side of the landslide (in the S80°E direction). This may be attributed to the presence of farmland and gully topography in the area. The high water content in this area may have further enhanced the weathering of the underlying rock,

resulting in variations in the depth of the bottom boundary. Additionally, several zones of high V_x were detected in the profile, which are preliminarily interpreted as corresponding to moderately weathered tuff boulders, with borehole data confirming diameters ranging from 0.7 to 2.1 m. The presence of these boulders adds complexity to the hydro-mechanical properties within the soil layer, which may impact the stability of the landslide.

(3) Completely weathered tuff layer ($350 \text{ m/s} < V_x < 400 \text{ m/s}$): The D1-D3 profiles reveal pronounced heterogeneity in this layer, with localized zones exhibiting low V_x values (<250 m/s). These velocities are comparable to, or slightly higher than, those of the overlying soils. Borehole data (Fig. 12c) confirm that this unit consists of extremely soft rock, characterized by fragmented, loose structures and poor mechanical strength. A thin slip zone (0.5 m thick) typically separates this layer from the overlying residual clayey soil, aligning well with in-situ monitoring results and the inferred geometry of the failure surface

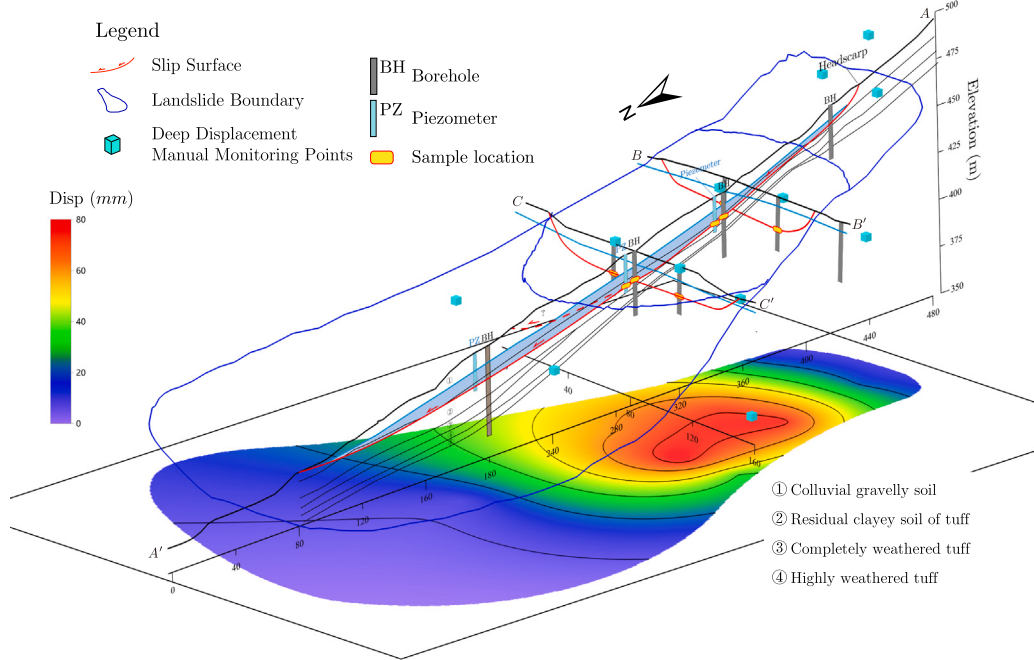


Fig. 9. Geological profile of the main sliding surface A-A' in the landslide deformation zone, with the distribution of sliding surfaces on sections B-B' and C-C'.

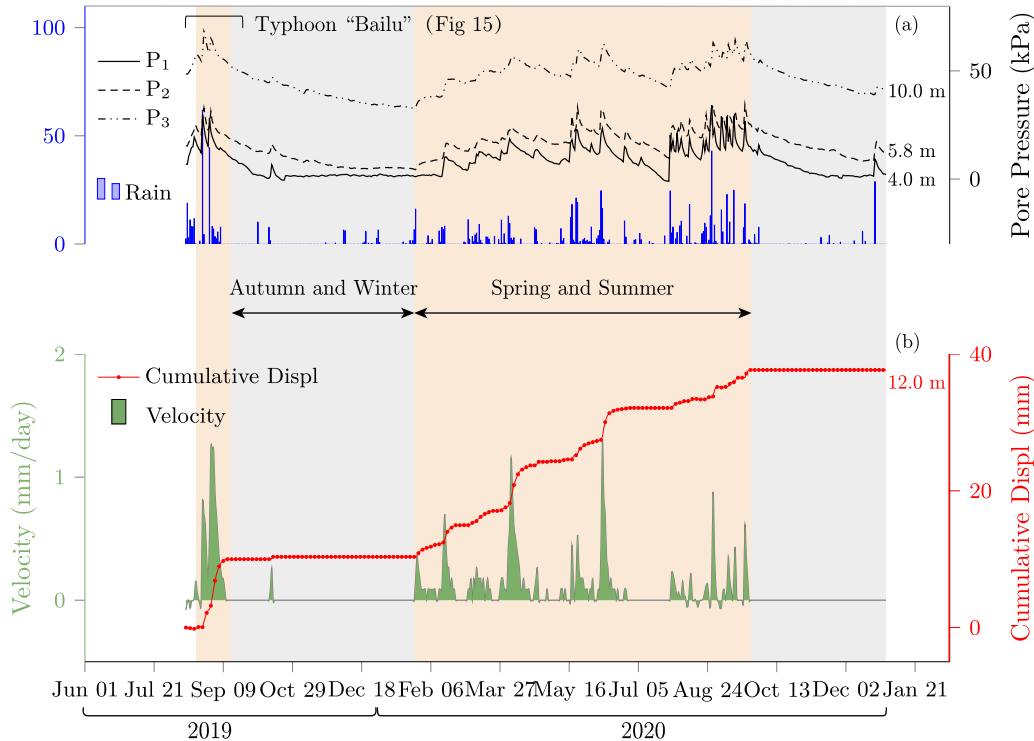


Fig. 10. Monitoring data from the Yaoshan landslide MS-1 station over different periods: (a) Response of pore water pressure at different depths to rainfall events; (b) Impact of different hydrological conditions on the landslide displacement rate.

(Fig. 12a, b). The high frequency of low V_x anomalies in this layer – more than in the residual soil – suggests reduced stability and increased susceptibility to sliding, supporting its identification as the principal sliding surface.

(4) Highly to moderately weathered tuff layer ($V_x > 400$ m/s): This rock layer remains largely intact compared to the overlying strata, with the original rock structure still distinctly visible. However, the layer exhibits significant undulations and convex features, which are

consistent with the fragmentation and significant lithological changes that occur in tuff following strong to moderate weathering. While the layer is generally more intact, localized areas of heterogeneity still exist.

In the 2D MSM profiles, variations in V_x primarily reflect differences in mineral composition and structural integrity of the subsurface materials. In particular, V_x is strongly correlated with the weathering degree of the tuff layer, ranging from completely weathered to

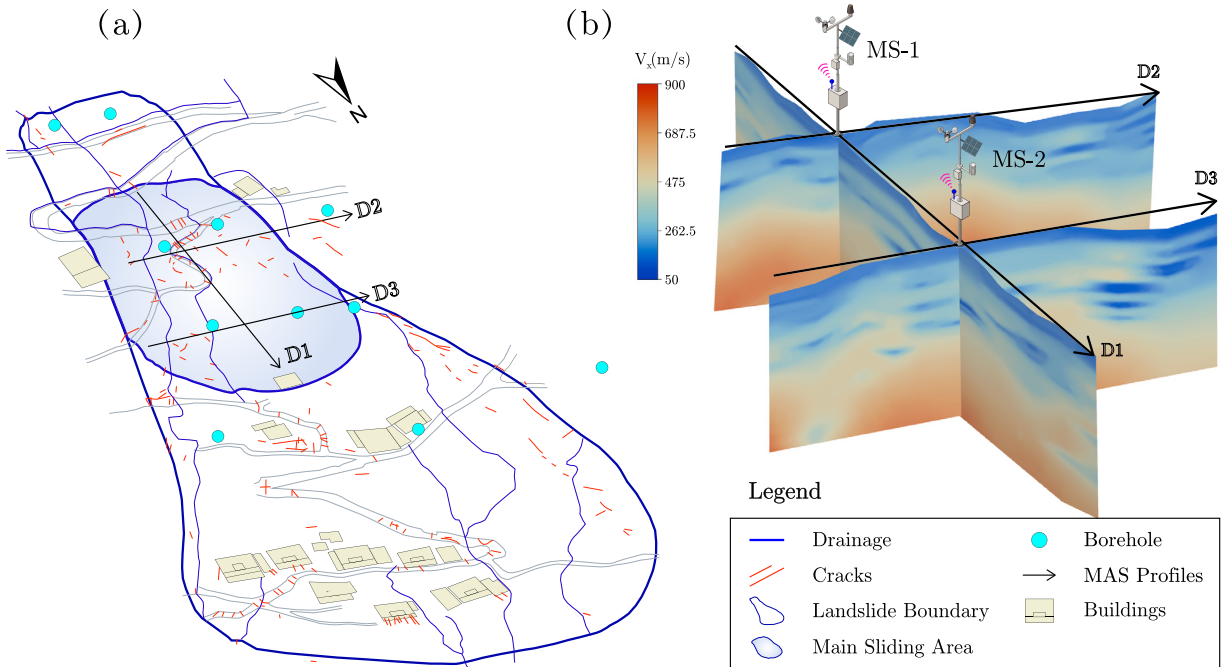


Fig. 11. (a) Locations of geophysical survey profiles D1-D3, with the main sliding zone shaded in blue. Topographical features as indicated in the legend of Fig. 1. (b) Three-dimensional view of the three microtremor V_x profiles and the location. (For interpretation of the references to color in this figure legend, the reader is referred to the web version of this article.)

unweathered states. Depth and moisture content further influence V_x values. Integrating MSM data with borehole observations allows for the effective delineation of weathering zones, enabling the identification of weak interlayers, fracture zones, large boulders, and potential slip surfaces (Xu et al., 2012). The strong agreement between the MSM inversion results, borehole data, and field observations confirms the reliability and accuracy of the interpretation.

4.2.2. Key subsurface structural features

In landslides, soil deformation generally occurs near the sliding surface, interfaces, or weak interlayers. Significant changes in shear wave velocity in these areas can indicate potential failure surfaces. Thus, analyzing shear wave velocity in landslides is essential for extracting key information about the slip surface, such as its geometry and depth, and identifying potential critical subsurface features.

Profiles D2 and D3 (oriented S80°W-S80°E) are situated beneath gullies G1 and G2, within the middle reaches of these gullies (Fig. 11a). The D3 profile (Fig. 12b) reveals significant variations in depth in the moderately weathered tuff layer, with depths significantly varying from 3 to 9 m over a short distance. The variations in weathering intensity have led to the formation of a bowl-shaped depression in the central part of the deformation zone. This depression can be considered a potential sliding surface and an active groundwater zone. The low permeability of the rock layers in this area probably contributes to the formation of the depression, which may trap water and cause pore water pressure to build up, leading to instability during or after heavy rainfall events.

A distinct vertical low-velocity zone U (<250 m/s) was observed on both sides of the D3 profile, beneath gullies G1 and G2, extending from the surface to depths of 10 m (U1) and 15 m (U2). These low-velocity zones (U1, U2) gradually develop downward and tend to connect with the central low-velocity zone U3 in the D3 profile. As discussed in the section on deep deformation characteristics, the landslide body, especially in the main sliding zone (II), has experienced significant deformation over time. This has probably exacerbated structural failure near the sliding zone. The depth range of 16–17 m (Fig. 8c CX9)

aligns exactly with the depth where a significant jump in V_x was observed. Additionally, the gullies maintain perennial water flow, with a discharge rate of approximately 150–300 m^{3/d}. This indicates that the cluster of low shear wave velocity zones (U) may be attributed to structural damage from landslide movement or continuous erosion induced by groundwater flow associated with G1 and G2. These zones could serve as potential pathways for underground water migration, channeling rainwater collected at the surface from the sides of the gully toward the bowl-shaped depression at the center. Moreover, the sliding zone in the D3 profile is more distinctly defined compared to the D2 profile, indicating a stronger hydrological response in the main sliding area and more intense slope deformation.

Fig. 12a shows the V_x profile D1 along the main direction of the landslide, approximately N10°E. The profile reveals significant variations in V_x between 12 m and 18 m within the landslide body, with numerous concentrated low-velocity zones below the slope. These zones connect to create a low-velocity band (V1, V2) extending 20 to 50 m, with velocities ranging from 150–250 m/s. Additionally, within the 65–118 m section of profile D1, V2 displays a bowl-shaped depression, corresponding to the D3 profile, suggesting a potential sliding surface. The alignment of this low-velocity band with sudden cumulative displacement observed at 12 m and 16.5 m, i.e., at monitoring points MS-1 and MS-2, supports the MSM results. Since these anomalies may be linked to the mechanism of intermittent landslide movement, we will explore this further in the discussion section, incorporating data from in-situ monitoring.

The MSM results revealed critical subsurface features of the landslide not observed in previous boreholes, enhancing the information obtained from the limited borehole and monitoring data. Additionally, MSM identified critical areas in the landslide deformation zone, such as bowl-shaped features and potential preferential hydrological pathways. These findings guided the planning of further field measurements using more expensive techniques and methods in landslide investigation. Overall, MSM is highly valuable for the investigation of landslides in complex terrains, offering essential insights into the internal structure of the landslide, especially critical features that are crucial for understanding the evolution mechanisms of landslide movement.

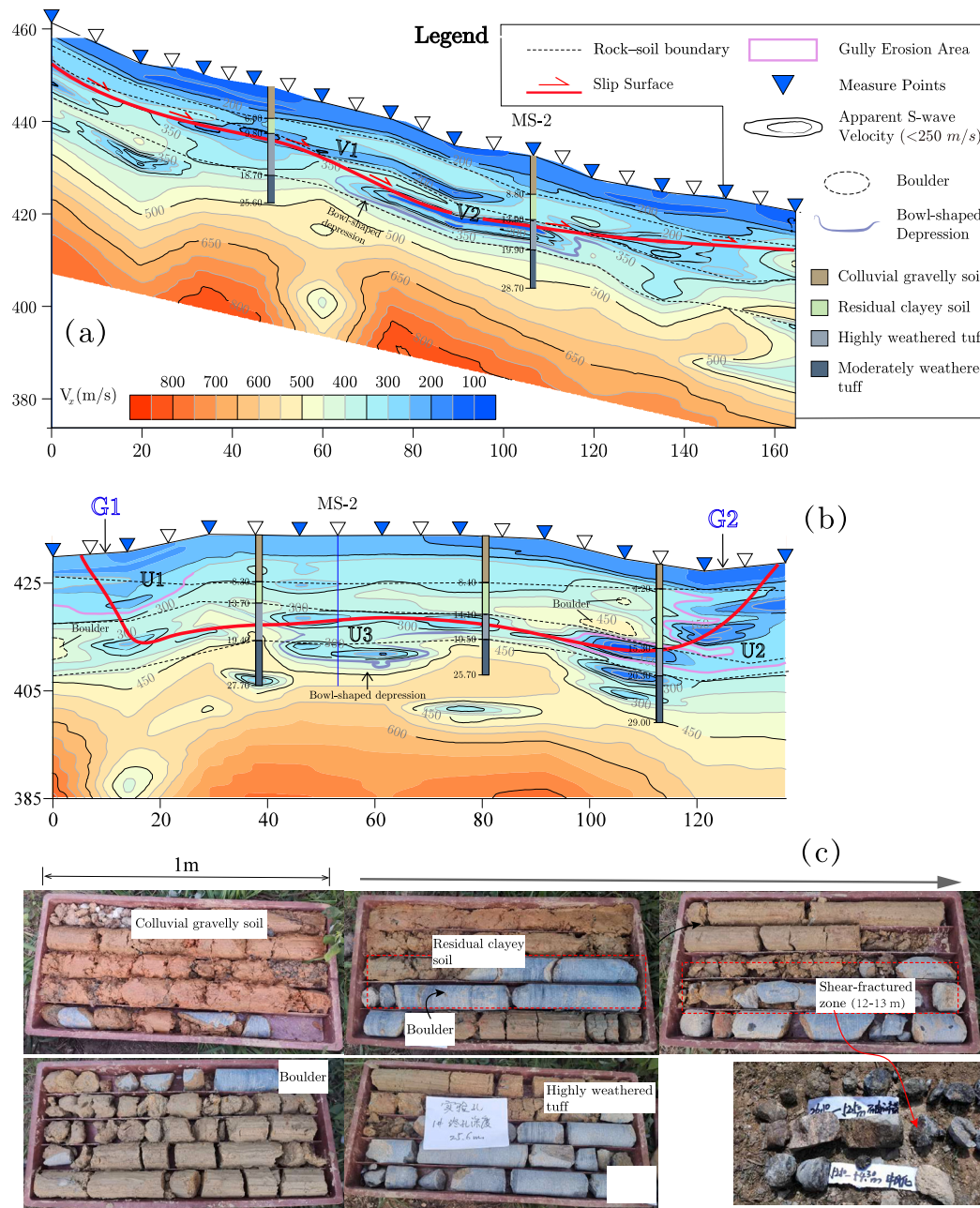


Fig. 12. (a), (b) Interpretation of the 2D microtremor V_x profiles D1 and D3, respectively. (c) Photographs of the rock and soil layers exposed by boreholes.

5. Discussion

5.1. Apparent S-wave velocity anomaly zones

Landslides frequently lead to variations in the mechanical and hydrogeological properties of surface and internal structures, which can alter their geophysical characteristics. The most significant feature of the 2D apparent S-wave velocity profile of the Yaoshan landslide is the presence of horizontal zones with anomalously low V_x (less than 250 m/s) at depths greater than 10 m. These zones extend 20 to 50 m in length and 3 to 5 m in thickness, often connecting one with the other. Several potential explanations could account for the presence of these low-shear wave velocity regions:

(1) **Material fragmentation and disturbance.** The Yaoshan landslide, situated in the hilly region of southeastern Fujian, China,

has experienced prolonged typhoon-induced heavy rainfall. This has led to an increase in pore pressure within the slope and a reduction in effective stress within the sliding zone (Fig. 13a). Consequently, these conditions have led to intermittent sliding and degradation of the rock and soil internal structure, potentially resulting in adjacent cracks slipping and expanding, or even leading to the rupture of intact rock and soil masses (Fig. 13b). This fragmentation and disturbance interfere with shear wave propagation, significantly reducing apparent S-wave velocity (Peng et al., 2017).

(2) **Cumulative damage effect.** Repeated landslide movements have led to a gradual accumulation of stress damage in the rock and soil mass within the sliding zone (Preisig et al., 2016). Each movement further fractures the rock and soil, resulting in microcracks and damage zones (Fig. 13c). These damaged areas

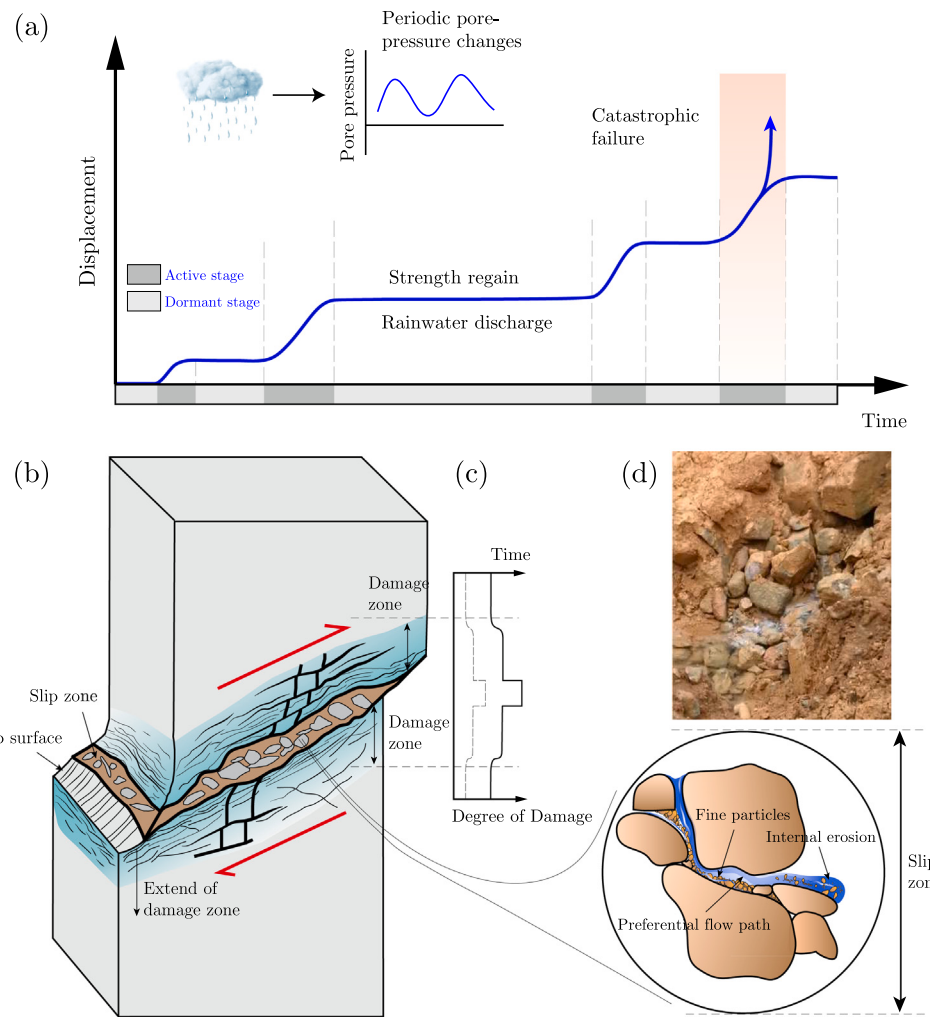


Fig. 13. (a) Schematic diagram of the Yaoshan landslide movement pattern. (b) Internal structural damage caused by landslide movement. (c) Cumulative stress damage due to repeated landslide movements. (d) Long-term seepage forming a network system and continuous erosion within the sliding zone.

- reduce the overall strength and stiffness of the material, leading to a decrease in apparent S-wave velocity (Rahimi et al., 2021).
- (3) **Internal water flow erosion.** Prolonged groundwater infiltration leads to a well-developed permeable network system along the sliding zone (Petrella et al., 2023; Hencher, 2010; Kang et al., 2022; Yang et al., 2024). This results in a continuous erosion of the internal structure of the soil layer. Additionally, perennial water flow in the gullies, coupled with long-term seepage through landslide debris, may accelerate internal erosion within the sliding zone (Fig. 13d). Fractures or voids within the rock and soil structure can also decrease wave velocity (Wei et al., 2021).
- (4) **Presence of liquid or saturation.** The central part of the landslide deformation zone is characterized by bowl-shaped depressions in the bedrock, which trap water and lead to fully saturated soil zones. The accumulation of pore pressure in these areas may lead to extremely low apparent S-wave velocity (Berti et al., 2019).

5.2. Hydrogeology and movement mechanism

Long-term hydrological conditions are critical to the unstable evolution of large deep-seated landslides induced by hydrological processes (Prokešová et al., 2013b; Gattinoni et al., 2012). Based on the

combined analysis of geological structure, hydrological conditions, and potential sliding surfaces, a schematic diagram (Fig. 14) was developed to illustrate the transmission of pore water pressure to the sliding zone through preferential hydrological pathways, triggering intermittent landslide movement. This schematic was developed using MSM, which revealed numerous apparent S-wave velocity anomalies (less than 250 m/s) in the V_x profile. These anomalies helped in identifying potential preferential hydrological pathways and permeable network systems, as well as determining the geometric shape of potential sliding surfaces. This schematic estimates the potential failure surface using engineering surveys and in-situ monitoring data.

In-situ hourly monitoring data (Fig. 15a) reveals that pore water pressure is strongly dependent on rainfall. Sensors P1 and P2, located at depths of 4 m and 5.8 m, respectively, respond rapidly to rainfall events, with changes occurring within an hour. These rapid fluctuations were associated with the fast wetting and drying of the colluvial gravel soil layer. On the contrary, pore water pressure at P3, located at a depth of 10 m beneath a relatively impermeable layer (residual clayey soil, $K_s = 1.01 \times 10^{-7}$ cm/s), responded very gradually but still within 2 h, indicating the water reaching deeper soil layers through preferential pathways (Fig. 15b). Additionally, the rate of pore water pressure fluctuation revealed that the pressure increased slightly faster than it decreased, suggesting that water infiltration and groundwater recharge in the deep landslide area were more efficient than water discharge.

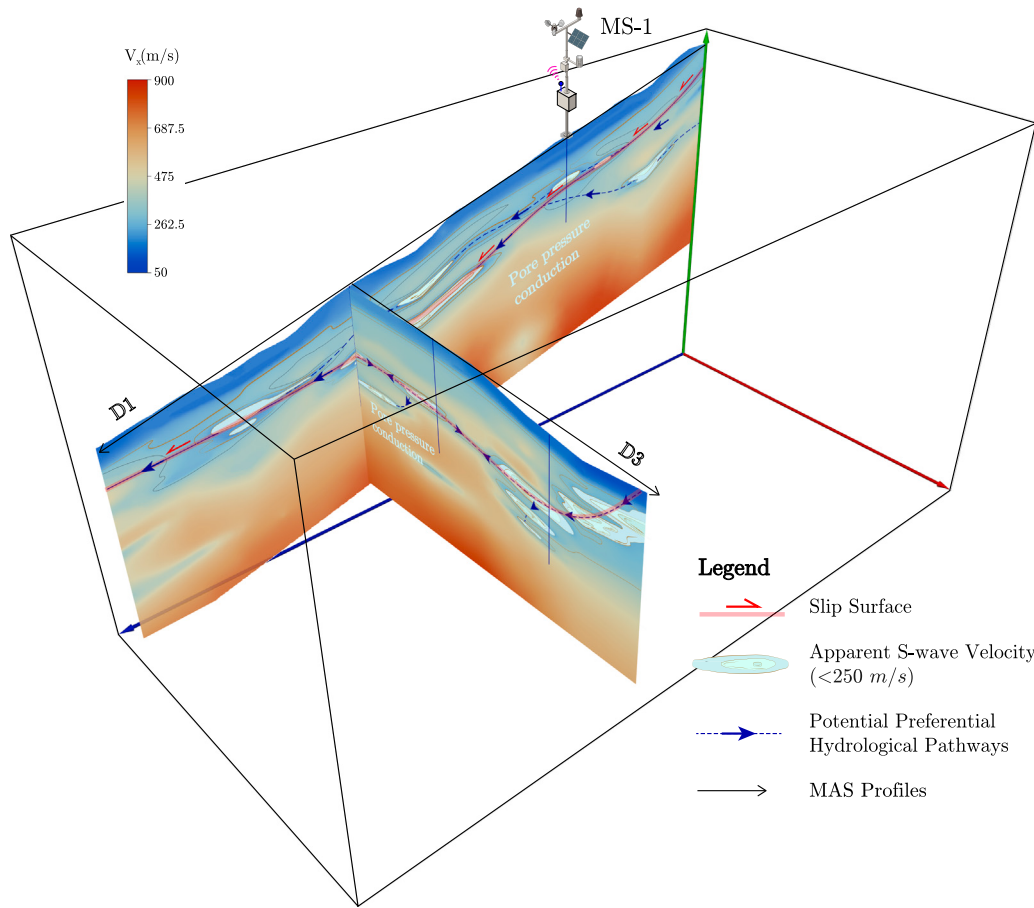


Fig. 14. Schematic diagram of pore water pressure transmission to the sliding zone through preferential hydrological pathways, triggering intermittent landslide movement.

This behavior is generally associated with preferential hydrological pathways, such as large pores, cracks, and soil pipes, which enhance the infiltration of rainwater and snowmelt (Bièvre et al., 2012; Prokešová et al., 2013b).

As shown in Fig. 14, at least two types of water circulation coexist within the Yaoshan landslide. The first involves a faster circulation, where rainfall rapidly infiltrates and flows through a well-connected network of large pores, cracks, and soil pipes. The second involves a deeper circulation, where water flows through the soil matrix and cracks within the landslide body. Groundwater flows along the sliding zone and adjacent cracks through zones of increased permeability, such as confined and artesian sections, and connects to the surface through erosion channels in the surrounding gullies. Due to their high permeability and the mobility of water, these preferential hydrological pathways can rapidly and significantly alter the hydraulic conditions within the landslide body during heavy rainfall events, thereby triggering landslide movement (Fig. 15a). Under long-term climatic fluctuations, such as repeated wet-dry cycles or sustained infiltration during the rainy season, these preferential pathways may evolve through internal erosion or structural degradation of sliding zone materials, leading to progressive damage to their internal structure (Xu et al., 2021; Xue et al., 2022; Liao et al., 2021; Miao et al., 2020). This process may weaken the interlocking and friction among soil particles, cause the loss of fine clay particles, and destroy arch-like soil structures, thereby increasing permeability and reducing residual strength (Wang et al., 2025).

Furthermore, compared with other landslides in similarly complex geological settings-characterized by heterogeneous subsurface structures and intricate hydrological features (Petrella et al., 2023)-such as the Montescaglioso landslide in southern Italy (Calamita et al., 2023a),

the L'ubietová landslide in central Slovakia (Prokešová et al., 2013b), and the Kunimi landslide in northern Japan (Shuzui, 2001), conventional approaches for identifying preferential hydrological pathways often rely on invasive borehole validation or face resolution limitations in vegetated and rugged terrain. In contrast, the application of MSM in this study significantly improves spatial resolution, reduces invasiveness, and enhances the detection of weak interlayers and internal discontinuities. These capabilities help overcome key limitations of traditional landslide monitoring techniques, which often fail to adequately capture the presence and influence of such pathways on the overall hydrogeological system. Consequently, the ability to detect and assess preferential flow paths is of great importance for understanding landslide hydrodynamics and plays a crucial role in predicting slope instability and designing effective risk mitigation strategies.

6. Conclusions

In this study, an in-depth investigation of the large landslide body in Yaoshan Village, Anxi County, China, was conducted using geophysical techniques in combination with extensive field surveys. By combining MSM with in-situ monitoring data, we gained new insights into the mechanism driving intermittent landslide movement. The major conclusions drawn from this study are as follows:

(1) Long-term in-situ monitoring enabled visualization of the overall three-dimensional deformation of the Yaoshan landslide, revealing its spatiotemporal dynamics and resulting in the division of the landslide into three zones: traction zone, main sliding zone, and resistance zone. The periodic fluctuations in pore pressure along the sliding surface can be attributed to seasonal changes in groundwater recharge, leading to intermittent movement characterized by phases of acceleration

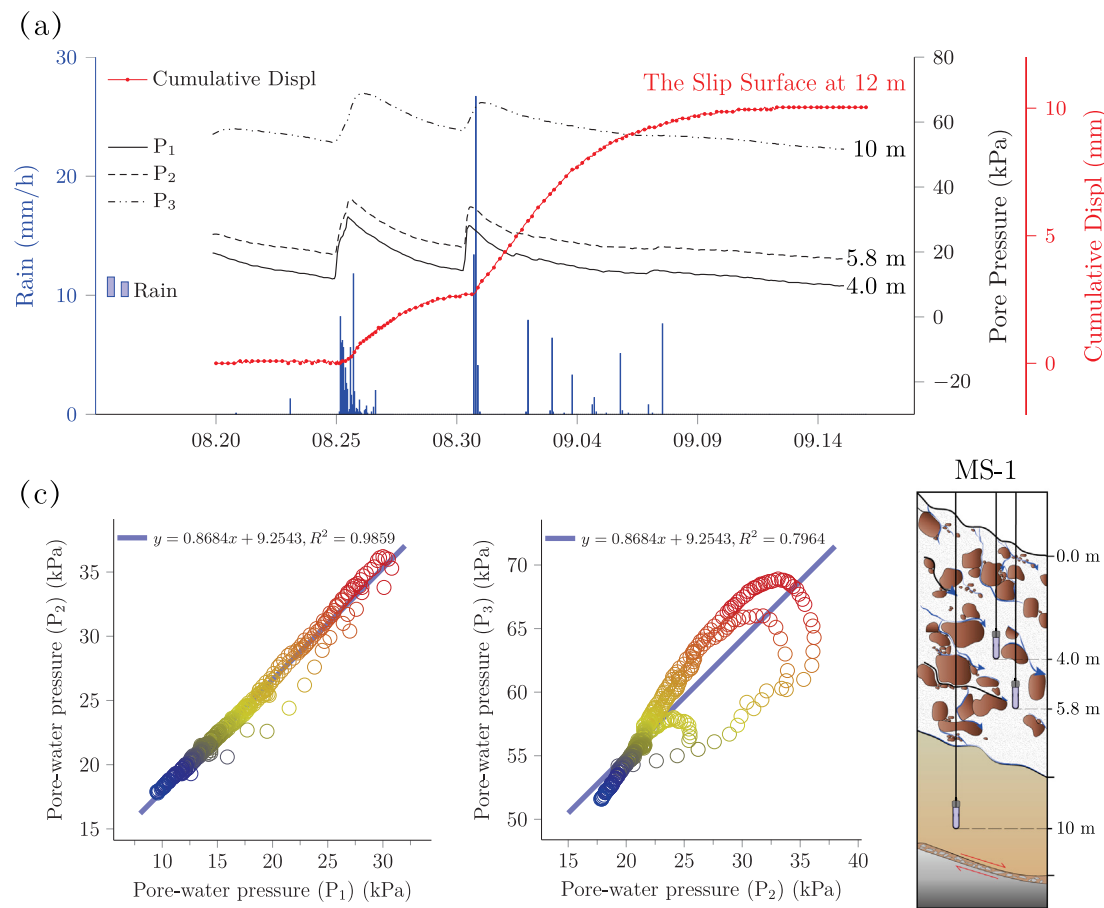


Fig. 15. (a) The relationship between landslide movement, pore water pressure, and rainfall at monitoring point MS-1 during typhoon Bailu's landfall at the Yaoshan landslide. (b) The response relationship between pore water pressure P1, P2 and P2, P3.

and deceleration. This movement pattern is controlled by the interaction between the sliding surface morphology, the complex subsurface hydrological system, and the geological structural features.

(2) In the selected main sliding area of the landslide, three two-dimensional V_x profiles were generated using a two-dimensional microtremor array technique, enabling the detailed reconstruction of the internal structure of the landslide body. By integrating existing borehole data, the depth and spatial distribution of the sliding surface were comprehensively analyzed, resulting in the delineation of the lithological layers. These interpretations exhibited a high level of consistency with exposed surface profiles and monitoring data.

(3) Research indicated that the bowl-shaped features within the rock layers may play a crucial role in driving the movement of the Yaoshan landslide. These features develop due to the low permeability of the rock layers, leading to infiltrating rainfall being trapped and rapidly accumulating within the bowl-shaped zones. This results in the buildup of pore water pressure within the sliding zone, which can trigger landslide movement. These critical features are frequently overlooked in lithological profiles interpreted solely based on borehole data.

(4) This study has further enhanced the conceptual hydrogeological model of the Yaoshan landslide by combining V_x profiles with multi-source in-situ monitoring data. The zones of low V_x anomaly have been identified as potential preferential hydrological pathways. It is hypothesized that there are at least two groundwater circulation patterns within the landslide: one involving rainfall infiltrating and flowing through a high-permeability network of large pores, fractures, and soil pipes; and another involving water flowing directly to the sliding zone

through erosion channels in the gullies. These preferential hydrological pathways can rapidly and substantially change the hydraulic conditions within the landslide body, thereby triggering landslide movement.

Briefly, the 2D microtremor detection results demonstrate that the 2D microtremor array technique provides significant advantages in landslide geological disasters, especially in areas with complex and uneven terrain. Its ease of deployment and adaptability make it a valuable supplementary tool in landslide surveys. A significant limitation of existing landslide investigation methods is their lack of spatial information on the internal structural characteristics of the landslide area. This information is crucial for understanding seepage pathways and the mechanisms driving landslide movement.

CRediT authorship contribution statement

Jian Yang: Writing – original draft, Visualization, Methodology, Investigation. **Huiqi Zhang:** Visualization, Investigation, Formal analysis. **Wenbin Jian:** Writing – review & editing, Funding acquisition, Conceptualization. **Lipeng Lin:** Methodology, Investigation. **Luis F. Robledo:** Writing – review & editing. **Hao Wang:** Writing – review & editing, Resources. **Hongqiang Dou:** Writing – review & editing.

Declaration of competing interest

The authors declare the following financial interests/personal relationships which may be considered as potential competing interests: Jian Wenbin reports financial support was provided by National Natural Science Foundation of China.

Acknowledgments

The authors are grateful to the financial supports from National Natural Science Foundation of China (NSFC-CONICYT, U2005205; 41861134011).

Data availability

Data will be made available on request.

References

- Aki, K., 1957. Space and time spectra of stationary stochastic waves, with special reference to microtremors. *Bull. Earthq. Res. Inst.* 35, 415–456.
- Berti, M., Bertello, L., Squarzoni, G., 2019. Surface-wave velocity measurements of shear stiffness of moving earthflows. *Landslides* 16 (3), 469–484. <http://dx.doi.org/10.1007/s10346-018-1102-1>.
- Bièvre, G., Jongmans, D., Winiarski, T., Zumbo, V., 2012. Application of geophysical measurements for assessing the role of fissures in water infiltration within a clay landslide (Trièves area, french alps). *Hydrol. Process.* 26 (14), 2128–2142. <http://dx.doi.org/10.1002/hyp.7986>.
- Calamita, G., Gallipoli, M., Gueguen, E., Sinisi, R., Summa, V., Vignola, L., Stabile, T., Bellanova, J., Piscitelli, S., Perrone, A., 2023a. Integrated geophysical and geological surveys reveal new details of the large Montescaglioso (southern Italy) landslide of December 2013. *Eng. Geol.* 313, 106984. <http://dx.doi.org/10.1016/j.enggeo.2023.106984>.
- Calamita, G., Gallipoli, M.R., Gueguen, E., Sinisi, R., Summa, V., Vignola, L., Stabile, T.A., Bellanova, J., Piscitelli, S., Perrone, A., 2023b. Integrated geophysical and geological surveys reveal new details of the large Montescaglioso (Southern Italy) landslide of December 2013. *Eng. Geol.* 313, 106984. <http://dx.doi.org/10.1016/j.enggeo.2023.106984>.
- Carey, J.M., Massey, C.I., Lyndsell, B., Petley, D.N., 2019. Displacement mechanisms of slow-moving landslides in response to changes in porewater pressure and dynamic stress. *Earth Surf. Dyn.* 7 (3), 707–722. <http://dx.doi.org/10.5194/esurf-7-707-2019>.
- Dai, L., Fan, X., Wang, D., Zhang, F., Yunus, A.P., Subramanian, S.S., Rogers, J.D., Havenith, H.-B., 2023. Electrical resistivity tomography revealing possible breaching mechanism of a late pleistocene long-lived gigantic rockslide dam in Diexi, China. *Landslides* 20 (7), 1449–1463. <http://dx.doi.org/10.1007/s10346-023-02048-0>.
- Fabbrocino, S., Lanzano, G., Forte, G., Santucci de Magistris, F., Fabbrocino, G., 2015. SPT blow count vs. Shear wave velocity relationship in the structurally complex formations of the molise region (Italy). *Eng. Geol.* 187, 84–97. <http://dx.doi.org/10.1016/j.enggeo.2014.12.016>.
- Gattinoni, P., Scesi, L., Arieni, L., Canavesi, M., 2012. The February 2010 large landslide at Maierato, Vibo Valentia, Southern Italy. *Landslides* 9 (2), 255–261. <http://dx.doi.org/10.1007/s10346-011-0296-2>.
- Handwerger, A.L., Roering, J.J., Schmidt, D.A., 2013. Controls on the seasonal deformation of slow-moving landslides. *Earth Planet. Sci. Lett.* 377, 239–247. <http://dx.doi.org/10.1016/j.epsl.2013.06.047>.
- Hasan, M., Shang, Y., Yi, X., Shao, P., He, M., 2023. Determination of rock mass integrity coefficient using a non-invasive geophysical approach. *J. Rock Mech. Geotech. Eng.* 15 (6), 1426–1440. <http://dx.doi.org/10.1016/j.jrmge.2022.07.008>.
- Hencher, S.R., 2010. Preferential flow paths through soil and rock and their association with landslides. *Hydrol. Process.* 24 (12), 1610–1630. <http://dx.doi.org/10.1002/hyp.7721>.
- Huang, R., Li, W., 2011. Formation, distribution and risk control of landslides in China. *J. Rock Mech. Geotech. Eng.* 3 (2), 97–116. <http://dx.doi.org/10.3724/SP.J.1235.2011.00097>.
- Kamiński, M., Zientara, P., Krawczyk, M., 2021. Electrical resistivity tomography and digital aerial photogrammetry in the research of the “Bachledzki hill” active landslide – in podhale (Poland). *Eng. Geol.* 285, 106004. <http://dx.doi.org/10.1016/j.enggeo.2021.106004>.
- Kang, X., Wang, S., Wu, W., Xu, G., Zhao, J., Liu, F., 2022. Soil–water interaction affecting a deep-seated landslide: From field monitoring to experimental analysis. *Bull. Eng. Geol. Environ.* 81 (2), 1–16. <http://dx.doi.org/10.1007/s10064-021-02556-0>.
- Krzeminska, D., Bogaard, T., Malet, J.-P., Van Beek, L., 2013. A model of hydrological and mechanical feedbacks of preferential fissure flow in a slow-moving landslide. *Hydrol. Earth Syst. Sci.* 17 (3), 947–959. <http://dx.doi.org/10.5194/hess-17-947-2013>.
- Lacroix, P., Handwerger, A.L., Bièvre, G., 2020. Life and death of slow-moving landslides. *Nat. Rev. Earth Environ.* 1 (8), 404–419. <http://dx.doi.org/10.1038/s43017-020-00072-8>.
- Li, X., Xuan, Y., Zhou, X., Wang, X., Ouyang, G., Duan, J., Bo, J., 2024. Seismic effect of the Wangjiayan landslide based on microtremor measurements in Beichuan, Southwest China. *Landslides* 21 (4), 875–888. <http://dx.doi.org/10.1007/s10346-023-02191-8>.
- Liao, K., Wu, Y., Miao, F., Li, L., Xue, Y., 2021. Time-varying reliability analysis of Majiagou landslide based on weakening of hydro-fluctuation belt under wetting-drying cycles. *Landslides* 18, 267–280. <http://dx.doi.org/10.1007/s10346-020-01496-2>.
- Ling, S., 1994. Research on the Estimation of Phase Velocities of Surface Waves in Microtremors. Hokkaido University, Sapporo (in Japanese).
- Liu, Q., Jian, W., Nie, W., 2021. Rainstorm-induced landslides early warning system in mountainous cities based on groundwater level change fast prediction. *Sustain. Cities Soc.* 69, 102817. <http://dx.doi.org/10.1016/j.scs.2021.102817>.
- Lu, K., Li, F., Pan, J., Li, K., Li, Z., Wang, P., 2024. Structural characterization and attempted displacement interpretation of the baishuihe landslide using integrated geophysical methods. *Eng. Geol.* 336, 107568. <http://dx.doi.org/10.1016/j.enggeo.2024.107568>.
- Luo, S.-L., Jin, X.-G., Huang, D., 2019. Long-term coupled effects of hydrological factors on kinematic responses of a reactivated landslide in the three gorges reservoir. *Eng. Geol.* 261, 105271. <http://dx.doi.org/10.1016/j.enggeo.2019.105271>.
- Miao, F., Wu, Y., Li, L., Tang, H., Xiong, F., 2020. Weakening laws of slip zone soils during wetting–drying cycles based on fractal theory: a case study in the Three Gorges Reservoir (China). *Acta Geotech.* 15, 1909–1923. <http://dx.doi.org/10.1007/s11440-019-00894-8>.
- Nappo, N., Peduto, D., Mavrouli, O., van Westen, C.J., Gullà, G., 2019. Slow-moving landslides interacting with the road network: Analysis of damage using ancillary data, in situ surveys and multi-source monitoring data. *Eng. Geol.* 260, 105244. <http://dx.doi.org/10.1016/j.enggeo.2019.105244>.
- Okada, H., 2006. Theory of efficient array observations of microtremors with special reference to the SPAC method. *Explor. Geophys.* 37 (1), 73–85. <http://dx.doi.org/10.1071/EG06073>.
- Osawa, H., Matsushi, Y., Matsuura, S., Okamoto, T., 2023. Semiempirical modeling of the transient response of pore pressure to rainfall and snowmelt in a dormant landslide. *Landslides* 21 (2), 245–256. <http://dx.doi.org/10.1007/s10346-023-02158-9>.
- Pazzi, V., Morelli, S., Fanti, R., 2019. A review of the advantages and limitations of geophysical investigations in landslide studies. *Int. J. Geophys.* 2019 (1), 2983087. <http://dx.doi.org/10.1155/2019/2983087>.
- Peng, J., Wang, G., Wang, Q., Zhang, F., 2017. Shear wave velocity imaging of landslide debris deposited on an erodible bed and possible movement mechanism for a loess landslide in Jingyang, Xi'an, China. *Landslides* 14 (4), 1503–1512. <http://dx.doi.org/10.1007/s10346-017-0827-6>.
- Perrone, A., Canora, F., Calamita, G., Bellanova, J., Serlenga, V., Panebianco, S., Tragni, N., Piscitelli, S., Vignola, L., Doglioni, A., Simeone, V., Sdao, F., Lapenna, V., 2021. A multidisciplinary approach for landslide residual risk assessment: The pomarico landslide (basilicata region, Southern Italy) case study. *Landslides* 18 (1), 353–365. <http://dx.doi.org/10.1007/s10346-020-01526-z>.
- Petrella, E., Raimondo, M., Chelli, A., Valentino, R., Severini, E., Diena, M., Celico, F., 2023. Processes and factors controlling the groundwater flow in a complex landslide: A case study in the northern Italy. *Hydrol. Process.* 37 (5), e14891. <http://dx.doi.org/10.1002/hyp.14891>.
- Preisig, G., Eberhardt, E., Smithyman, M., Preh, A., Bonzanigo, L., 2016. Hydromechanical rock mass fatigue in deep-seated landslides accompanying seasonal variations in pore pressures. *Rock Mech. Rock Eng.* 49 (6), 2333–2351. <http://dx.doi.org/10.1007/s00603-016-0912-5>.
- Prokešová, R., Medveďová, A., Tábořík, P., Snopková, Z., 2013b. Towards hydrological triggering mechanisms of large deep-seated landslides. *Landslides* 10, 239–254. <http://dx.doi.org/10.1007/s10346-012-0330-z>.
- Rahimi, S., Wood, C.M., Bernhardt-Barry, M., 2021. The MHVSR technique as a rapid, cost-effective, and noninvasive method for landslide investigation: Case studies of Sand Gap and Ozark, AR, USA. *Landslides* 18 (8), 2705–2720. <http://dx.doi.org/10.1007/s10346-021-01677-7>.
- Rahimi, S., Wood, C.M., Coker, F., Moody, T., Bernhardt-Barry, M., Mofarragh Kouchaki, B., 2018. The combined use of MASW and resistivity surveys for levee assessment: A case study of the Melvin price reach of the Wood River Levee. *Eng. Geol.* 241, 11–24. <http://dx.doi.org/10.1016/j.enggeo.2018.05.009>.
- Roberts, J., Asten, M., 2005. Estimating the shear velocity profile of Quaternary silts using microtremor array (SPAC) measurements. *Explor. Geophys.* 36 (1), 34–40. <http://dx.doi.org/10.1071/EG05034>.
- Shuzui, H., 2001. Process of slip-surface development and formation of slip-surface clay in landslides in Tertiary volcanic rocks, Japan. *Eng. Geol.* 61 (4), 199–220. [http://dx.doi.org/10.1016/S0013-7952\(01\)00025-4](http://dx.doi.org/10.1016/S0013-7952(01)00025-4).
- Skepton, A.W., Hutchinson, J.N., 1969. Stability of natural slopes and embankment foundations. In: Inglis, C.C. (Ed.), *Soil Mechanics*. Butterworths, London, pp. 291–340.

- Su, L., Xu, X., Geng, X., Liang, S.-q., 2017. An integrated geophysical approach for investigating hydro-geological characteristics of a debris landslide in the Wenchuan Earthquake Area. *Eng. Geol.* 219, 52–63. <http://dx.doi.org/10.1016/j.enggeo.2016.11.020>.
- Wang, Q., Tang, H., An, P., Fang, K., Zhou, B., Zhang, X., 2025. Shear strength and permeability in the sliding zone soil of reservoir landslides: Insights into the seepage-shear coupling effect. *J. Rock Mech. Geotech. Eng.* 17 (4), 2031–2040. <http://dx.doi.org/10.1016/j.jrmge.2024.04.033>.
- Wei, Z., Chu, R., Li, Z., Sheng, M., Zeng, Q., 2021. Poisson's ratios and S-wave velocities of the Xishancun Landslide, Sichuan, China, inferred from high-frequency receiver functions of local earthquakes. *Sci. China Earth Sci.* 64 (7), 1195–1206. <http://dx.doi.org/10.1007/s11430-020-9734-5>.
- Xu, P., Ling, S., Li, C., Du, J., Zhang, D., Xu, X., Dai, K., Zhang, Z., 2012. Mapping deeply-buried geothermal faults using microtremor array analysis. *Geophys. J. Int.* 188 (1), 115–122. <http://dx.doi.org/10.1111/j.1365-246X.2011.05266.x>.
- Xu, X.-t., Shao, L.-j., Huang, J.-b., Xu, X., Liu, D.-q., Xian, Z.-x., Jian, W.-b., 2021. Effect of wet-dry cycles on shear strength of residual soil. *Soils Found.* 61 (3), 782–797. <http://dx.doi.org/10.1016/j.sandf.2021.03.001>.
- Xu, X.-q., Su, L.-j., Zhang, G.-d., Zhu, H.-h., 2017. Analysis on shear wave velocity structure of a gravel landslide based on dual-source surface wave method. *Landslides* 14 (3), 1127–1137. <http://dx.doi.org/10.1007/s10346-016-0780-9>.
- Xue, Y., Miao, F., Wu, Y., Dias, D., 2022. Dynamic stability assessment of reservoir colluvial landslide using a hypoplastic clay constitutive model considering the effects of drying-wetting cycles on the hydro-fluctuation belt. *Eng. Geol.* 307, 106791. <http://dx.doi.org/10.1016/j.enggeo.2022.106791>.
- Yang, J., Huang, Z., Jian, W., Robledo, L.F., 2024. Landslide displacement prediction by using Bayesian optimization-temporal convolutional networks. *Acta Geotech.* 19 (7), 4947–4965. <http://dx.doi.org/10.1007/s11440-023-02205-8>.
- Zhang, Y., Ren, S., Liu, X., Guo, C., Li, J., Bi, J., Ran, L., 2023. Reactivation mechanism of old landslide triggered by coupling of fault creep and water infiltration: A case study from the East Tibetan Plateau. *Bull. Eng. Geol. Environ.* 82 (8), 291. <http://dx.doi.org/10.1007/s10064-023-03290-5>.
- Zhuang, Y., Xing, A., Jiang, Y., Sun, Q., Yan, J., Zhang, Y., 2022. Typhoon, rainfall and trees jointly cause landslides in coastal regions. *Eng. Geol.* 298, 106561. <http://dx.doi.org/10.1016/j.enggeo.2022.106561>.
- Zhuang, Y., Xing, A., Sun, Q., Jiang, Y., 2023. Insights into initiation of typhoon-induced deep-seated landslides in Southeast Coastal China. *Nat. Hazards* 119 (1), 721–749. <http://dx.doi.org/10.1007/s11069-023-06138-z>.